nature nanotechnology

LETTERS

PUBLISHED ONLINE: 20 DECEMBER 2009 | DOI: 10.1038/NNANO.2009.454

New modes for subsurface atomic force microscopy through nanomechanical coupling

L. Tetard[1,2], A. Passian[1,2]* and T. Thundat[1,2]

Non-destructive, nanoscale characterization techniques are needed to understand both synthetic and biological materials. The atomic force microscope uses a force-sensing cantilever with a sharp tip to measure the topography and other properties of surfaces[1,2]. As the tip is scanned over the surface it experiences attractive and repulsive forces that depend on the chemical and mechanical properties of the sample. Here we show that an atomic force microscope can obtain a range of surface and subsurface information by making use of the nonlinear nanomechanical coupling between the probe and the sample. This technique, which is called mode-synthesizing atomic force microscopy, relies on multi-harmonic forcing of the sample and the probe. A rich spectrum of first- and higher-order couplings is discovered, providing a multitude of new operational modes for force microscopy, and the capabilities of the technique are demonstrated by examining nanofabricated samples and plant cells[3,4].

To understand materials, it is important to be able to examine surface and subsurface domains for the presence of inhomogenities in a non-invasive manner. Inspired by earlier work on ultrasonic microscopy[5,6], ultrasonic force microscopy was introduced by Quate and colleagues[7], and Kolosov and colleagues[8] in the early 1990s. Since then, various nanomechanical analogues of heterodyning (hereafter termed generally 'ultrasonic microscopy') have appeared in various works, including those of Cuberes and colleagues[9] and Shekhawat and colleagues[10]. Ultrasonic microscopy has also recently been used to visualize carbon nanohorns[11] and silica nanoparticles[12] buried in a mouse macrophage.

In dynamic atomic force microscopy (AFM)[2,13–15], a silicon microcantilever, a mechanical oscillator with frequency f_p, interacts with a surface of interest by means of a van der Waals potential (and often with contributions from other interactions including thermomolecular, electrostatic and Casimir) prevailing in the nanometre interfacial region between the surface $\bar{r}_s$ and the cantilever probe tip $\bar{r}_L$, as partially shown in Fig. 1. In ultrasonic microscopy[11], the (sample) surface may be considered to constitute a second mechanical oscillator, with a frequency f_s resulting from a force exerted on the sample by the ultrasonic vibrations of a piezoelectric material at the contact interface (Fig. 1). An image may then be acquired from the phase of a signal, resulting from locking onto the cantilever motion with reference to the difference between the sample and probe frequencies[11,12]. Here, we introduce the concept of mode-synthesizing atomic force microscopy (MSAFM), and show that signal transduction and image formation can occur in an expanded frequency space by using a multiple-order coupling (see Supplementary Section S2), symbolically denoted by $\mathcal{C}$, which is solely induced by the nonlinear probe–surface interaction. We then show that $\mathcal{C}$, provided by the much faster (compared to the excitation timescales) interfacial electronic interactions, allows synthesis of a multitude of new operational modes, or $\mathcal{C}$-modes, limited only by the system and measurement bandwidth. The vast dynamic landscape of $\mathcal{C}$ renders MSAFM drastically different from existing modalities. To manage the synthesized modes, we first introduce a Dirac-like notation (see Supplementary Section S2) for the states of the system ($\mathcal{C}$-modes) and arrange these in a Groterian-like diagram (Fig. 2). Finally, the utility of MSAFM as a novel modality of subsurface and surface force microscopy is demonstrated, first by imaging nanofabricated, structurally simple samples (see Supplementary Section S4), and then by studying the remaining problem of the cellular level compositional variations of poplar wood cross-sections (see Supplementary Section S5)[16].

MSAFM is based on exerting a multi-harmonic force $F_s = \Sigma_j a_{s,j} \sin(2\pi f_{s,j} t + \varphi_{s,j})$ on the substrate, and another $F_p = \Sigma_i a_{p,i} \sin(2\pi f_{p,i} t + \varphi_{p,i})$ on the probe (see Supplementary Section S2), such that when the probe–sample separation d ($=|\bar{r}_L - \bar{r}_s|$) is reduced below a threshold value, the nonlinear probe–sample

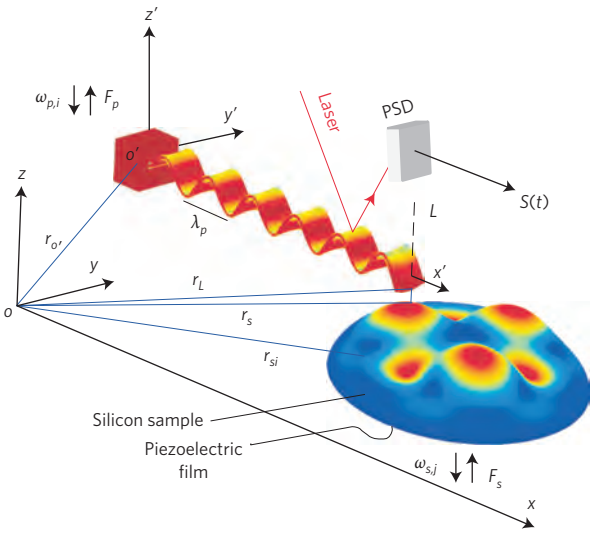

Figure 1 | Probe–sample interaction in MSAFM. Computed eigenmodes of a silicon microcantilever and a silicon sample. The left boundary of the cantilever probe (length L) is fixed with respect to the origin $r_{o'}$ of the accelerated reference frame o' x' y', but oscillates with respect to the inertial reference frame oxy (see Supplementary Section S1). The probe and the sample are driven by piezoelectric films exerting forces F_p and F_s, respectively, resulting in the excitation of an elastic mode of the sample and the probe. The motion of the sample at r_s is measured with respect to oxy. A laser and a position-sensitive detector (PSD) represent the dynamics of the system in the time domain by $S(t)$. An embedded inhomogeneity at r_{si} modifies the dynamics of r_s affecting the signal $S(t)$ through the coupling $\mathcal{C}$ (see Supplementary Section S3). The wavelength of the high-frequency ω_p oscillations of the cantilever is denoted by λ_p.

[1]Oak Ridge National Laboratory, Oak Ridge, Tennessee 37831-6123, USA, [2]Department of Physics, University of Tennessee, Knoxville, Tennessee 37996, USA. *e-mail: passianan@ornl.gov

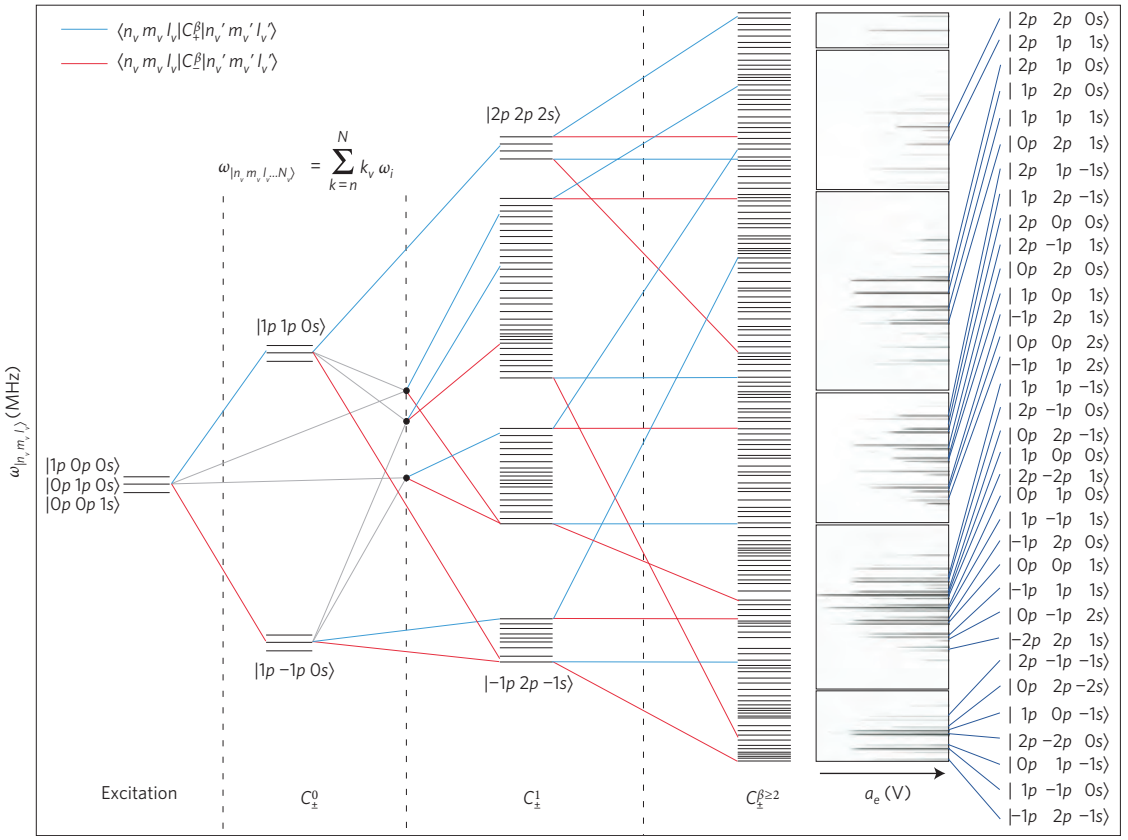

Figure 2 | Multiple orders coupling in frequency space during MSAFM. This three-stimuli diagram represents all the dynamic states created by $\mathcal{C}$. The three excitations (two for the probe and one for the sample) listed in the first column, the initial states of the system, are mixed by $\mathcal{C}$ to theoretically generate six new states by the first-order coupling $\mathcal{C}^0$, 62 states for the second-order coupling $\mathcal{C}^1$, and so on. A spectral contour plot of the measured $a_{|nml\rangle}$ (where n, m, $l = -2, -1, \ldots, 1, 2$, and i is a position counter in the sum symbol) with $a_{|001_s\rangle} = a_{|01_p0\rangle} = a_{|1_p00\rangle} = a_e$ containing 34 selected states, which can all be used simultaneously for imaging, is presented in the last column.

interaction $\mathcal{C} \neq 0$ creates a time domain signal $S(t)$ that represents the dynamic state of the probe, as annotated in Fig. 1. To describe systematically the synthesized modes, we may, somewhat metaphorically, resort to an atomic analogue for the coupled system. For example, in a hydrogen atom, the electron and the nucleus, constituting the two oscillators, interact via a Coulomb potential to generate the discrete quantum states $|nlm\rangle$. In the case of MSAFM, where the probe and the sample constitute the two oscillators, they interact by means of a van der Waals potential to generate the well-defined states $|n_v m_v l_v \ldots\rangle$. The number of excitation states determines the number of integers (n_v, m_v, l_v, ...) that will populate a given state $|\cdot\rangle$. Then, assigning n, m, l, $\ldots = 0, \pm 1, \pm 2, \ldots$, and an index $v = s, p$, where s and p refer to the sample, and the probe, we define $|n_v m_v l_v, \ldots\rangle$ to be a state with a frequency $\omega_{|n_v m_v l_v, \ldots\rangle} = n_v\omega_{v,1} + m_v\omega_{v,2} + l_v\omega_{v,3} + \cdots$ and an amplitude $a_{|n_v m_v l_v, \ldots\rangle}$, where $\omega_{v,i} = 2\pi f_{v,i}$. Now, symbolically representing each Fourier component of S as $|n_v m_v l_v \ldots\rangle$, MSAFM uses the amplitude and phase of $S(t)$ by simultaneously locking onto the frequency of any given number of $\mathcal{C}$-modes, that is, $\omega_{|n_v m_v l_v, \ldots\rangle}$. For example, in Fig. 2 (see also Supplementary Fig. S6), we consider three excitation states and the notation will take the form $|\cdot\rangle = |n_v m_v l_v\rangle$. Similarly, in Fig. 3 and Fig. 4, the measurements present results from exciting the system at two frequencies, in which case $|\cdot\rangle = |n_v m_v\rangle$. Note that $\mathcal{C} \to 0$ in the limit of large d, and each oscillator will possess a spectrum originating from its own driving frequency tuning (see Supplementary Section S1), that is, ω_s^q and ω_p^κ, $q = \kappa = 1, 2, \ldots, \infty$. For example, when $i = 1$, 2 and $j = 1$ in F_p and F_s, a striking 62 $\mathcal{C}$-modes are predicted as mapped in Fig. 2. Here, a selected 34 experimentally measured $\mathcal{C}$-modes are also shown, for which the contour plots in the fifth column collectively represent the measured amplitudes $a_{|n_v m_v l_v, \ldots\rangle}$ as a function of the amplitude of the excitations. The first-order coupling $\mathcal{C}^0$ mixes the three excitation modes $|0_p 0_p 1_s\rangle$, $|0_p 1_p 0_s\rangle$ and $|1_p 0_p 0_s\rangle$ to give rise to six modes via sum and difference generation, whereas the second-order coupling $\mathcal{C}^1$ mixes the previous modes to create the 62 modes by further sum and difference generation, and so on. Thus, the coupling may be viewed as an operator reinforced as $\mathcal{C}_\pm^\beta$ to signify the order β and sum/difference operation performed on the states $|n_v m_v l_v, \ldots\rangle$, as annotated in Fig. 2. Consequently, $\mathcal{C}$ may be envisioned as being analogous to the susceptibility χ in nonlinear optics[17], albeit the role of a material nonlinear polarizability is played by the nonlinear interfacial forces in MSAFM. Juxtaposition of the modes in the proposed Groterian-like diagram, in fact surpasses a simple storing utility. The diagram clearly keeps track of whether a given mode is a result of a summation or subtraction, and whether the mode is a result of a first coupling or a higher-order coupling. In addition, it also includes information about the origin of the excitation ($v = p$ for probe, s for sample). Furthermore, the modes are vertically dispersed according to their frequency.

The parameter dependencies of $\mathcal{C}$ may be unveiled, for example for the simplest case of $i = j = 1$, by studying $\mathcal{C} = \mathcal{C}$ ($f_{p,1}$, $f_{s,1}$, $a_{p,1}$, $a_{s,1}$, d). Note first that the first-order nonlinear coupling between $|0_s 1_p\rangle$ and $|1_s 0_p\rangle$ will create two states: $\langle 1_s 0_p | \mathcal{C}_+^\beta | 0_s 1_p \rangle = |1_s 1_p\rangle$ for the sum, and $\langle 1_s 0_p | \mathcal{C}_-^\beta | 0_s 1_p \rangle = |-1_s 1_p\rangle$ for the difference. For fixed and equal driving amplitudes $a_{p,1} = a_{s,1}$, the experimental measurements are shown in Fig. 3 for the spectral and amplitude dependencies of the selected $\mathcal{C}$-modes $|nm\rangle = |-1_s 1_p\rangle$ (Fig. 3a),

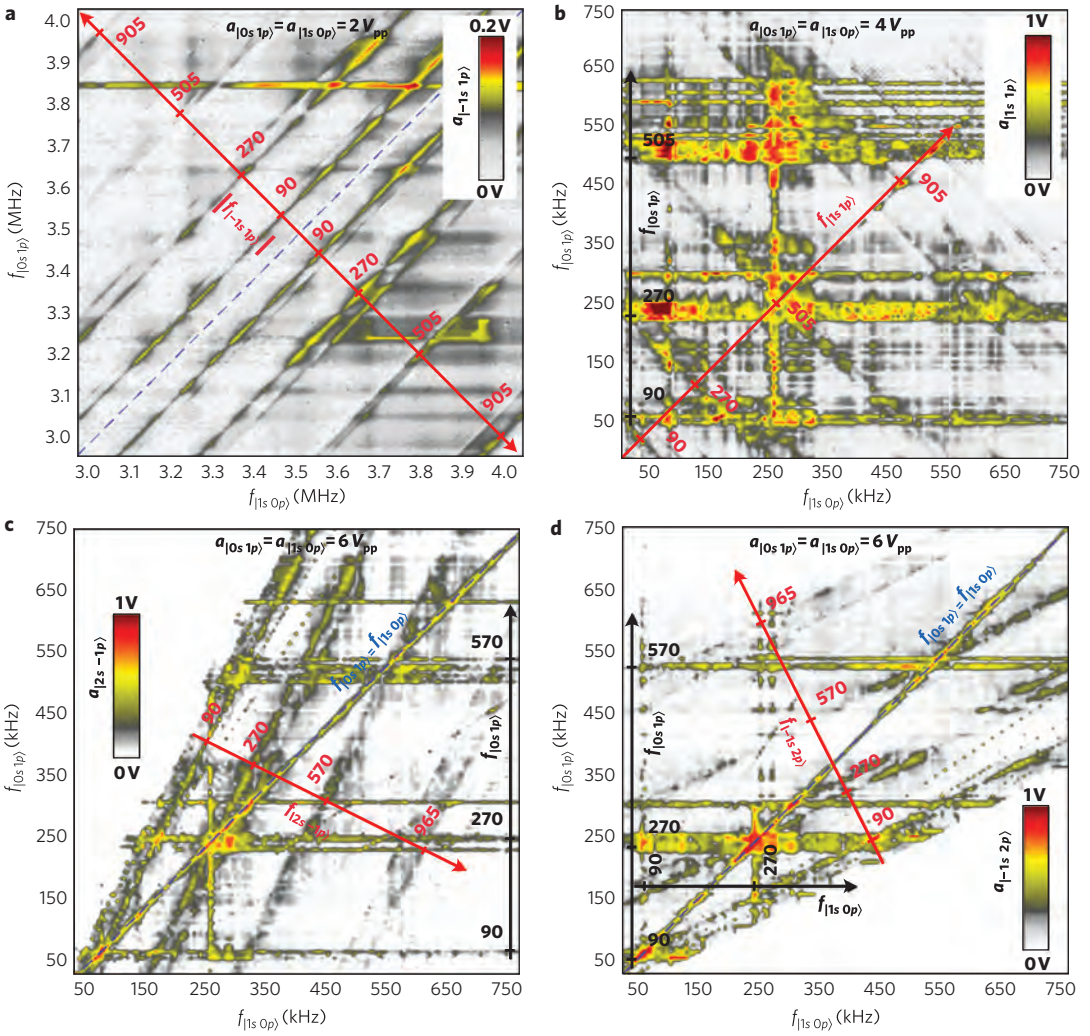

Figure 3 | Parameter dependence of selected $\mathcal{C}$-modes. **a**, Variation of the amplitude of the $\mathcal{C}^0$-mode $|-1_s1_p\rangle$ in the higher-frequency excitation. **b**, Lower-frequency amplitude dependence of the $\mathcal{C}^0$-mode $|1_s1_p\rangle$ at higher excitation amplitudes. **c**,**d**, Dependence of selected $\mathcal{C}^1$-modes on excitation frequency at higher excitation amplitudes. In all, red and black axes mark the occurrence of ω_p^κ, and the blue axes demarcate the equality of excitation frequencies. The excitation amplitudes are annotated on the top portion and a scale bar is provided to categorize the contour levels. The exhibited bands can be identified to correspond to (in-contact) ω_p^κ, $\kappa = 1, 2, \ldots$.

$|1_s1_p\rangle$ (Fig. 3b), $|2_s-1_p\rangle$ (Fig. 3c), and $|-1_s2_p\rangle$ (Fig. 3d). The observed bands correspond to $\omega_{|nm\rangle} = \omega_p^\kappa$, with the values corresponding to the first few modes κ annotated (see Supplementary Section S1). The vertical lines formed in Fig. 3 are indicative of a maximum in the displacement of the cantilever at any of the $\omega_{|nm\rangle}$ when the driving frequency applied to the probe corresponds to one of the ω_p^κ (see Methods).

To demonstrate how MSAFM successfully accesses new dimensions of sample information, we use two sets of $\mathcal{C}$-modes to image a sample made of nickel nanostructures confined in a germanium coating on a quartz substrate (see Supplementary Section S4 and Fig. S3), and a second sample composed of the poorly understood cross-sections of poplar wood (see Methods and Supplementary Section S5). In the first set, shown in Fig. 4a–d, the participant modes were selected to be $|nm\rangle = |-1_s1_p\rangle$ (Fig. 4a,e), $|-1_s2_p\rangle$ (Fig. 4b,e), $|1_s1_p\rangle$ (Fig. 4c,e), and $|0_s2_p\rangle$ (Fig. 4d,e) originating from $i = j = 1$, while Fig. 4g–j displays images acquired by $|nm\rangle = |-1_p1_p\rangle$ (Fig. 4g,f), $|2_p-1_p\rangle$ (Fig. 4h,f), $|-1_p2_p\rangle$ (Fig. 4i,f), and $|0_p2_p\rangle$ (Fig. 4j,f) originating from $i = 1, 2$, and $j = 0$ (that is, no subsurface contribution) (see Supplementary Sections S2, S4 and S5). A remarkable diversity in the gained information can readily be observed in these results. We emphasize that the information in any one image cannot simply be generated by a scaling or a transformation from another image, and that each $\mathcal{C}$-mode taps into an auxiliary dimension of information space of the sample. Thus, MSAFM, in a single run, yields a detailed manifold and takes advantage of the true dynamic richness of the nonlinear interaction. The set of $\mathcal{C}$-modes engaged in image formation can readily be adjusted, as shown in the study of a poplar cell wall (Supplementary Fig. S6) for the case with $i = 1, 2$ and $j = 1$.

In conclusion, we have described a new modality of force microscopy that can be of significant importance for nanoscale characterization of material. Using nonlinear interactions, in a single run, MSAFM is capable of delivering myriad (Figs. 2 to 4) nanoscale features not attainable by other means. Controlled use of the synthesized modes for surface and subsurface characterization of a structurally simple nanofabricated sample and poplar cells demonstrates the versatility of the presented methodology and suggests a potential application in studying complex samples such as an organic system that shows a variety of interrelated chemical, morphological and mechanical properties, as opposed to simple samples characterized rather with homogeneity, uniformity and isotropicity. The experimental observation that the force is not maximum at the collapse point of the probe implies that both

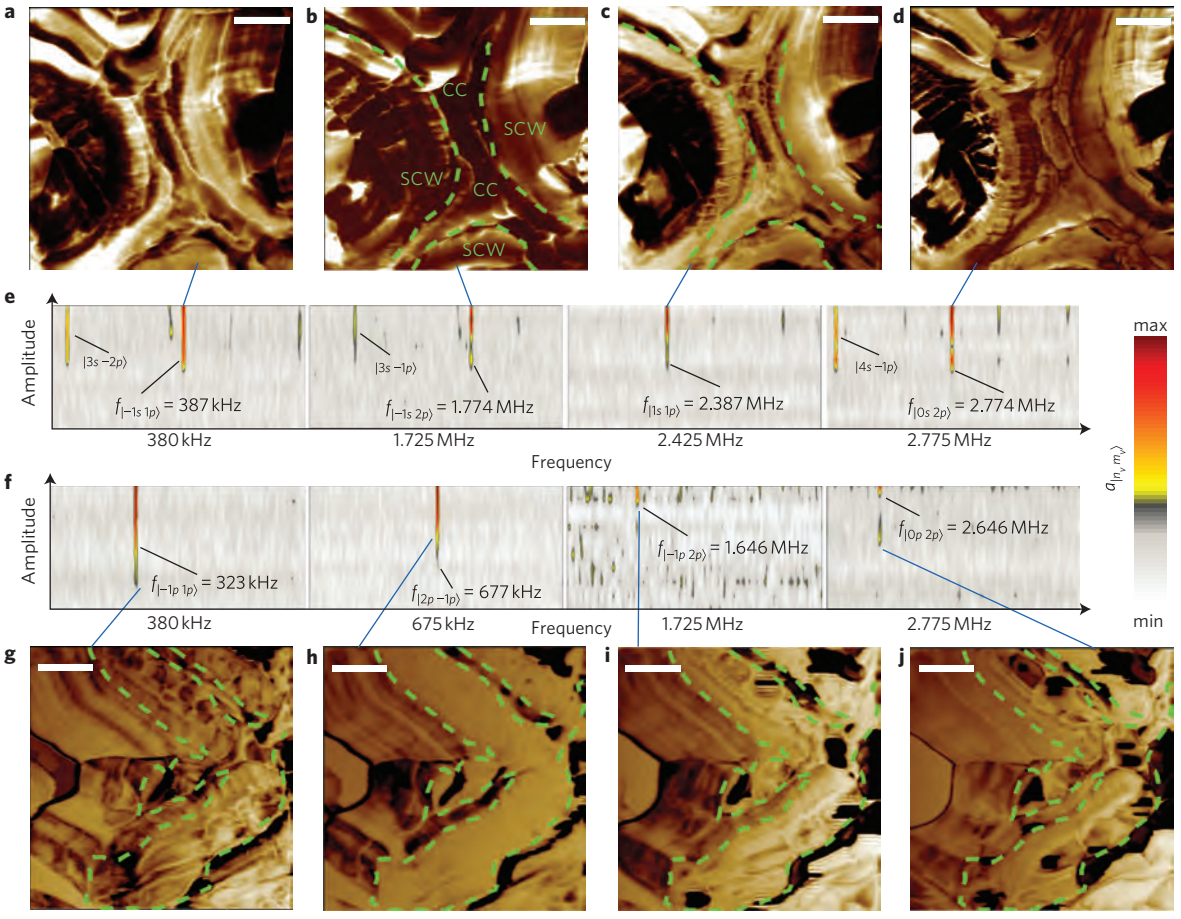

Figure 4 | Analysis of cross-sections of fresh poplar wood with MSAFM. a–d, Simultaneous $\mathcal{C}$-mode imaging of a poplar sample resolving the various layers of the cell walls. The secondary cell wall (SCW), the cell corner (CC) and the middle lamella (L) reveal distinct features of the complex organic matrix. Scale bars are 2 μm. **e**, Contour plots of partial spectral windows containing the invoked $\mathcal{C}$-modes. The centre frequency for each window in **e** and **f** appears below the frequency axis. **f–j**, $\mathcal{C}$-modes from the excitation of the probe with two independent waves, but maintaining a stationary sample. The cell wall regions and the lamella can be identified from the complementary information contained by each image. Scale bars are 2 μm.

attractive and repulsive forces are at play under MSAFM. We have demonstrated that, within the measurement bandwidth, the $\mathcal{C}^{\beta}_{\pm}$ modes are all fully operational. MSAFM capitalizes on the full range of $\mathcal{C}$, and uses both amplitude and phase for image formation, so many opportunities remain to be explored. For example, further work on MSAFM will provide information on whether or not the observed states can be made coherent, opening up the opportunity for inventive phase measurements.

Methods

Populus section preparation. Populus or poplar is a woody plant belonging to the Salicaceae family[3]. This sample was chosen due to its importance in the scientific initiative of bioenergy production. Microtoming of poplar wood was performed at Georgia Institute of Technology (see Acknowledgments). The thickness of the samples varied from 10 to 50 μm. The cross-sections were prepared from fresh samples in both cases. Poplar samples, stored in a dry environment between two microscope glass slides to prevent distortion, were then immobilized on a substrate using an adhesive film typically used in scanning electron microscopy.

AFM modification and instrumentation. Two piezoelectric (PZT) films (from Physik Instrumente model PIC255) were adapted to accommodate the cantilever probe and the sample. Both films were wire-bonded to accept multiple driving waves from the excitation voltage sources (Agilent 33120A). Using a network analyser (HP PSA Series E444XA), impedance measurements were carried out to obtain the frequency response of the PZTs and determine their resonances. This information was needed for the determination of the total experimental and measurement bandwidth. A commercial atomic force microscope (Veeco) with a Nanoscope III controller was used to acquire the results. A signal access module (Veeco), an oscilloscope with megahertz sampling rate (Agilent DSO5034A), and lock-in amplifiers (200 MHz SRS 844 and SRS 530), and a network analyser (HP 4195A) were used to carry out all the measurements. Instrument automation and control and data acquisition were implemented in Labview using GPIB communication.

Microcantilever probes. The AFM probes predominantly used were selected to have two different stiffnesses and geometries. The detailed computational results representing their eigenfrequencies and eigenmodes have been included in Suplementary Section S1. The soft probes with a triangular geometry (Veeco Probes DNP-S) and with a stiffness of 0.06 N m^{-1} were used for the measurements presented in Figs 2 and 3, whereas stiff cantilevers with rectangular geometries (Olympus model OMCL-AC160 TS-W2) were used for the measurements presented in Fig. 4. The soft cantilevers were made from silicon nitrite with a gold coating and the stiff cantilevers from silicon.

Experimental procedure and bandwidth limitation. Experimentally, using a laser and a position-sensitive detector (PSD), the dynamics of the microcantilever were extracted by measuring the instantaneous position of a segment of the cantilever, as denoted by $S(t)$ in Fig. 1. From the spectrum of the Brownian motion of the cantilever, or by explicit frequency sweeping of the voltage that drives the piezoelectric bimorph on which the cantilever rests, it can be readily observed[18] that all the eigenmodes κ undergo a redshift when d is reduced beyond some threshold (small shift in the case of a stiff cantilever). For the (contact mode) probes used here, the f^1_p shifted from 23 kHz to beyond the detection limit (collapsed mode), while f^2_p shifted from 130 kHz to 85 kHz, and so on. In our measurements, these spectral shifts, as well as force-curve behaviour did not exhibit a qualitatively strong dependence on the values of (f_p, f_s) and (a_p, a_s), except for the very large (a_p, a_s), where a maximum shift of about 1.5 kHz was measured (this may smear out the data in the (a_p, a_s) plane at higher ends because the lock-in is referenced at $\omega_{|n_v m_v l_v,\ldots\rangle}$). In our experiments, $\mathcal{C}$ could be measured over the entire frequency range, limited only by various bandwidths.

Note that the lock-in SR844 has a range of 25 kHz–200 MHz. Any reading from this lock-in, in the reference frequency window below 25 kHz, should be considered as out of range. To acquire data from this window, we used a different lock-in, the

SR530. In Fig. 3, the measurements show a coupling for $f_{|1_p-1_s\rangle} \approx 3$ kHz corresponding to $\omega_p{}^1$, that is, the first redshifted resonance of the probe.

Owing to the bandwidth limitation of the PSD (~1 MHz roll-off), an appropriate window for (f_s, f_p) has to be considered so that $S(t)$ will adequately contain information on $\omega_{|n_s m_s l_s \ldots\rangle}$. Also, because the piezoelectric crystals used do not have a flat spectrum in this window, certain amplitude-like variation in $\mathcal{C}$ is to be expected, as if (a_s, a_p) were varied. This was confirmed in our experiments by means of impedance measurements using a network analyser, yielding peaks of absorption at $f_s \approx 4.1$ MHz, and $f_p \approx 4.5$ MHz.

Received 17 April 2009; accepted 19 November 2009; published online 20 December 2009

References

1. Sahin, O. *et al.* An atomic force microscope tip designed to measure time-varying nanomechanical forces. *Nature Nanotech.* **2,** 507–514 (2007).
2. Garcia, R., Margerle, R. & Perez, R. Nanoscale compositional mapping with gentle forces. *Nature Mater.* **6,** 405–411 (2007).
3. Lynd, L. R. *et al.* How biotech can transform biofuels. *Nature Biotechnol.* **26,** 169–172 (2008).
4. Donohoe, B. S. *et al.* Visualizing lignin coalescence and migration through maize cell walls following thermochemical pretreatment. *Biotech. Bioeng.* **101,** 913–925 (2008).
5. Lemons, R. A. & Quate, C. F. Acoustic microscope—scanning version. *Appl. Phys. Lett.* **24,** 163–165 (1974).
6. Ilett, C., Somekh, M. G. & Briggs, G. A. D. Acoustic microscopy of elastic discontinuities. *Proc. R. Soc. Lond. A* **393,** 171–183 (1984).
7. Akamine, S., Hadimioglu, B., Khuri-Yakub, B. T., Yamada, H. & Quate, C. F. Acoustic microscopy beyond the diffraction limit: an application of microfabrication. *1991 Int. Conf. on Solid-State Sensors and Actuators, Digest of Technical Papers, Transducers '91*, 857–859 (1991).
8. Kolosov, O. *et al.* Nonlinear detection of ultrasonic vibrations in an atomic force microscope. *Jpn J. Appl. Phys.* **32,** L095–L098 (1993).
9. Cuberes, M. T., Assender, H. E., Briggs, G. A. D. & Kolosov, O. V. Heterodyne force microscopy of PMMA/rubber nanocomposites: nanomapping of viscoelastic response at ultrasonic frequencies. *J. Phys. D* **33,** 2347–2355 (2000).
10. Shekhawat, G. S. & Dravid, V. P. Nanoscale imaging of buried structures via scanning near-field ultrasound holography. *Science* **310,** 89–92 (2005).
11. Tetard, L. *et al.* Imaging nanoparticles in cells by nanomechanical holography. *Nature Nanotech.* **3,** 501–505 (2008).
12. Tetard, L. *et al.* Elastic phase response of silica nanoparticles buried in soft matter. *Appl. Phys. Lett.* **93,** 133113 (2008).
13. Lozano, J. R. & Garcia, R. Theory of phase spectroscopy in bimodal atomic force microscopy. *Phys. Rev. B* **79,** 014110 (2009).
14. Lozano, J. R. & Garcia, R. Theory of multifrequency atomic force microscopy. *Phys. Rev. Lett.* **100,** 076102 (2008).
15. Platz, D., Tholen, E. A., Pesen, D. & Haviland, D. B. Intermodulation atomic force microscopy. *Appl. Phys. Lett.* **92,** 153106 (2008).
16. Cosgrove, D. J. Growth of the plant cell wall. *Nature Rev. Mol. Cell Biol.* **6,** 850–861 (2005).
17. Boyd, R. W. *Nonlinear Optics* 2nd edn (Academic Press, 2002).
18. Rabe, U., Janser, K. & Arnold, W. Vibrations of free and surface-coupled atomic force microscope cantilevers: theory and experiment. *Rev. Sci. Instrum.* **67,** 3281–3293 (1996).

Acknowledgements

This research was sponsored by the Oak Ridge National Laboratory (ORNL) BioEnergy Science Center (BESC). The BioEnergy Science Center is a US Department of Energy (DOE) Bioenergy Research Center supported by the Office of Biological and Environmental Research in the DOE Office of Science. We are indebted to J. Seokwon and A. Ragauskas at the Georgia Institute of Technology for providing the poplar wood samples. We also thank B. Davison and M. Keller at ORNL for their support and useful discussions. ORNL is managed by UT-Battelle, LLC, for the US DOE under contract DE-AC05-00OR22725.

Author contributions

L.T., A.P. and T.T. designed and carried out the experiments, and wrote the manuscript.

Additional information

The authors declare no competing financial interests. Supplementary information accompanies this paper at www.nature.com/naturenanotechnology. Reprints and permission information is available online at http://npg.nature.com/reprintsandpermissions/. Correspondence and requests for materials should be addressed to A.P.